PHYSICAL REVIEW E **106**, 045111 (2022)

Contact line dynamics of a water drop spreading over a textured surface in the electrowetting-on-dielectric configuration

Raghvendra Kumar Dwivedi and K. Muralidhar*

Department of Mechanical Engineering Indian Institute of Technology Kanpur, Kanpur 208016, India

(Received 30 August 2022; accepted 10 October 2022; published 28 October 2022)

Modeling the electrowetting process of a liquid droplet placed on a hydrophobic surface in an ambient environment has several challenges over and above those of basic spreading [F. Mugele, Soft Matter **5**, 3377 (2009)]. At an external voltage below the value that causes contact angle saturation, transient spreading is augmented by contact angle reduction defined by the Young-Lippmann equation. In addition, the macroscopic equilibrium contact angle and, therefore, the spreading rate could be altered by the surface hysteresis. Beyond the saturation point, spreading reveals additional features of higher complexity [Q. Vo and T. Tran, J. Fluid Mech. **925**, A19 (2021)]. These details have been examined from experiments as well as numerical simulation in the present work. Below the saturation point, the contact angle model of Dwivedi *et al.* [Phys. Rev. Fluids **7**, 034002 (2022)] with the correction related to the electric field is seen to be applicable. Beyond saturation, the experimentally determined instantaneous contact angle distribution shows two distinct functionalities with respect to the contact line velocity. The first prevails from the onset of spreading until the spreading factor attains a peak value. The second trend is initiated with the retraction of the contact line. Except for differences in parametric values, the form of the contact angle model remains unchanged. Simulations in the postsaturation regime are shown to match experimental data in terms of the transient spreading factor, drop shapes, and the instantaneous contact angle. The role of the ground wire is found to be important and the three-phase contact line formed on it has been included in simulations. Spreading dynamics of the droplet have also been studied when the ground wire is kept at a distance of 40 μm from the apex of the drop. Simulations as well as experiments, show the propagation of a capillary wave between the ground wire and the three-phase contact line. For spreading over an uncoated polydimethylsiloxane (PDMS) surface, the contact line is trapped at local pinning sites, leading to additional distortions in the instantaneous shapes acquired by the interface.

DOI: 10.1103/PhysRevE.106.045111

I. INTRODUCTION

Electrowetting on dielectric (EWOD) is a promising technique to change the wetting behavior of a conducting drop placed over a dielectric coating. Starting with Lippmann's electrocapillarity experiment [1,2], several attempts have been made to understand the physics of contact angle reduction on a variety of surfaces. The electromechanical approach of Jones [3,4] examined the force exerted on the conducting droplet under electric field actuation. Vallet [5] used conformal mapping to determine the surface charge density distribution over the liquid-gas interface and showed divergence of the force field at the contact line. Adopting this approach, Kang [6] derived the form of the Young-Lippmann (YL) equation that is presently in use. A steady potential difference applied between a ground wire and an actuated electrode will increase the wettability of the conducting drop as per the Young-Lippmann equation given as [6]

$$\cos\theta_{\mathrm{YL}} = \cos\theta_e + \frac{\varepsilon\varepsilon_0 V^2}{2d\gamma}. \tag{1}$$

Here, θ_{YL} is the macroscopic contact angle of the droplet shape at equilibrium corresponding to V, an externally applied voltage. In addition, θ_e is the intrinsic equilibrium contact angle of the liquid relative to the surface, ε and d are the relative permittivity and the thickness of the dielectric layer respectively, γ is the liquid-air surface tension, and ε_0 is permittivity of free space. Further, it is expected that the charge redistribution occurs on a timescale of a few microseconds, leading to uniform potential distribution within the droplet.

Equation (1) is derived under the consideration of a perfect liquid conductor, smooth and homogeneous dielectric with permittivity equal to that of the surrounding liquid. The edge formed at the contact line is considered as an infinite planar wedge. Maxwell's stresses are taken to be distributed close to the contact line over a distance of order d and vanish rapidly beyond this region at the liquid-vapor interface. Thus, within a distance of $O(d)$, interface curvature balances the Maxwell stress distribution and the droplet shape matches Young's contact angle at the wall [7,8]. The interface shape follows the one predicted by the Young-Lippmann contact angle beyond a length scale of d/ε [7].

Figure 1(a) shows the configuration of a conducting liquid drop placed over a textured surface with a dielectric coating with the surrounding medium being air. The final shape of the drop under an electric field is shown by a thick line with θ_{YL}

---

*kmurli@iitk.ac.in

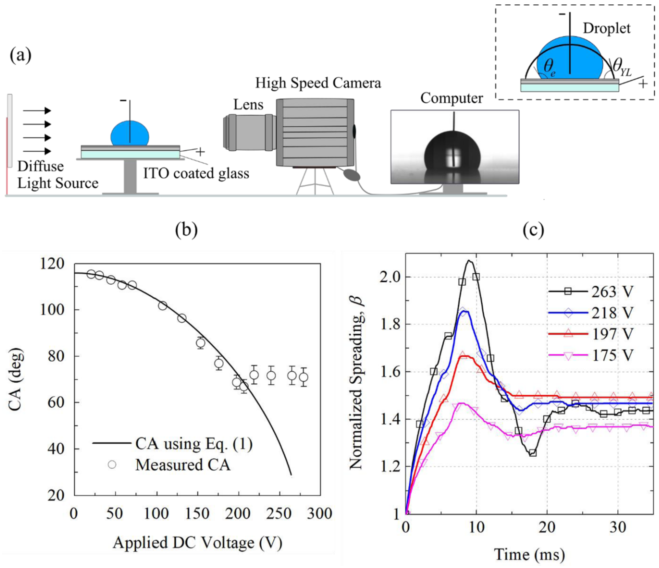

FIG. 1. (a) Schematic of the experimental setup. Over the ITO-coated glass, there is a dielectric layer of PDMS further coated with FluoroPel. The initial droplet shape is shown in blue with an equilibrium contact angle of θ_e. After applying the electric field, the drop is shown by a thick line with θ_{YL} as the macroscopic Young-Lippmann contact angle (boxed inset). A vertical wire of 0.07-mm diameter inserted into the drop serves as the ground electrode, whereas the top surface of ITO-coated glass serves as the actuated electrode. (b) Contact angle saturation (CAS) is observed when the applied voltage exceeds ∼200 V. (c) Variation of normalized spreading with time at various applied voltages. Beyond saturation, oscillations are set up during spreading. Normalization refers to the ratio of the instantaneous footprint diameter and the initial wetting diameter.

as the contact angle. As discussed in Ref. [9], finite hysteresis of the surface can cause the experimentally determined equilibrium contact angle (θ_f) at various voltages to differ from the Young-Lippmann value.

Equation (1), with V identified as the initial applied voltage, has been applied even during the spreading phase of the drop provided the ground wire continually remains in contact with the droplet. The transient evolution of the drop shape and the instantaneous footprint radius has been addressed in recent years by various researchers [10–13] where the Young-Lippmann contact angle is treated as the equilibrium limit. The effect of droplet volume and viscosity on spreading dynamics in an electric field has also been studied [9].

Drop spreading using EWOD has several applications in thermal management [14,15], water harvesting [16], self-cleaning [17], and digital microfluidics [18]. For patterned surfaces, it enhances the process capability by switching the wetting transition between Cassie and Wenzel states [19,20]. It has significant advantage in handling biological samples and reagents because of the absence of moving parts [18].

In spite of having several applications [21–25], EWOD-based technology is limited by contact angle saturation (CAS) [5,26,27]. This phenomenon relates to limits in increasing wettability beyond a certain voltage, consequently restricting the use of Eq. (1). Beyond the saturation level, the experimental value of the macroscopic contact angle starts deviating from the Young-Lippmann equation. For a water droplet of volume 6.5 μl placed on a FluoroPel-coated surface, contact angle saturation was seen to occur at around 200 V in the present work, as shown in Fig. 1(b). Oscillations induced in the drop beyond the saturation voltage are shown in Fig. 1(c) in terms of the normalized spreading parameter.

Several studies in the literature have addressed CAS [26,28–30] with a focus on experiments related to equilibrium shape attained in the postsaturation regime. Li *et al.* [31] show reduction in the saturation contact angle when charge trapping at the liquid-air interface is reduced. For a short duration, the instantaneous contact angle reaches a minimum and increases during contact line retraction. On reversal of voltage, contact angle diminishes again below its previous value. Vo *et al.* [32] examined the capillary wave propagation in an experiment where a water droplet is surrounded by silicone oil and the external voltage exceeds the CAS limit. The strength of the capillary wave is seen to increase with voltage. Experimentally, the initial spreading is seen to follow the Young-Lippmann theory for applied voltages even beyond the saturation limit.

In addition to the CAS mechanism, the dynamics of electrowetting in relation to surface texture has not been fully addressed. Several authors have included the model of hysteresis in the wall boundary condition [10,11]; however, its consequences at higher voltages is not understood. In addition, the presence of a ground electrode disturbs the hydrodynamics within the droplet during spreading by forming an extra three-phase contact line over it. In this connection, the effect of the ground wire can be minimized by working with a wire of small diameter, an approach followed by Vo *et al.* [32]. Further, drop spreading in air has numerous challenges related to three-phase contact line motion [7] since localized pinning sites act as energy barriers over the dry substrate. As a result, interfacial waves are formed and distort the drop-spreading process. Contact angle hysteresis on heterogeneous surfaces arises from contact line trapping, specifically over the groove parallel to the contact line [33]. Dwivedi *et al.* [34] considered local pinning and frictional losses during spreading over textured surfaces varying from hydrophilic to superhydrophobic. The model developed accounted for contact line pinning that resulted in late-stage droplet oscillations. Schneemilch *et al.* [35] studied steady contact line motion in electrowetting over a smooth cylindrical surface at nanoscale resolution.

The present study is intended to address the challenges in spreading over a textured surface in the EWOD framework when the surrounding fluid is air. The spreading factor, instantaneous contact angle distribution, and drop shapes are investigated. Numerical simulations are presented ahead of and beyond the CAS limit of an applied DC voltage. The applicability of the Young-Lippmann equation is investigated in these contexts. In addition, the effect of the position of the ground wire is examined in relationship to interfacial capillary waves at voltages beyond the saturation limit. EWOD experiments are performed first over a hydrophobic coating of FluoroPel, while PDMS is used as the dielectric layer. Secondly, experiments are carried out over a bare PDMS surface to bring in local energy barriers related to surface heterogeneity.

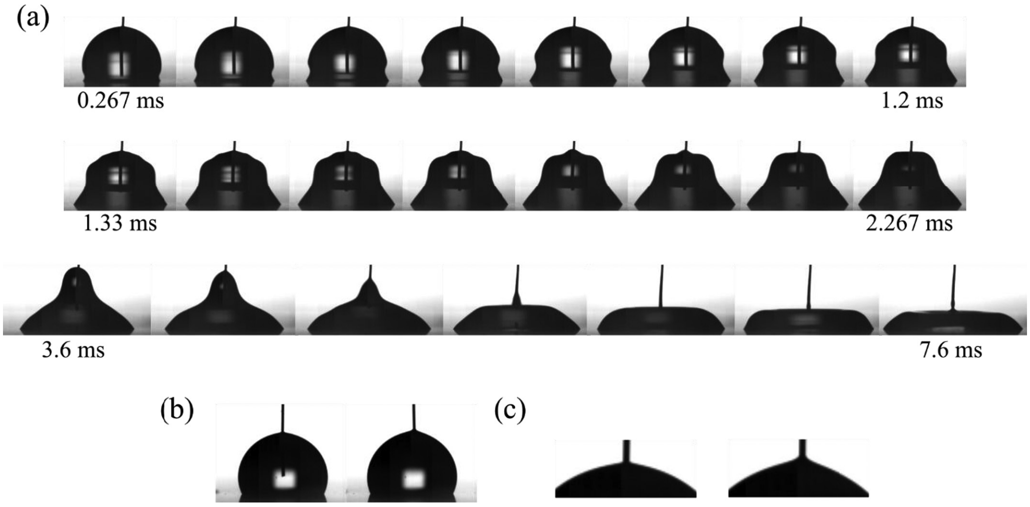

FIG. 2. (a) Interface shape of the drop is illustrated at 263 V when FluoroPel is used as the thin hydrophobic layer over PDMS. In the first and second rows, first image has a time stamp of 0.267 ms, and consecutive frames are separated by 0.133 ms. The third row shows the spreading regime with a time separation of 0.667 ms. (b) Shape of the water drop placed over the PDMS-coated ITO glass in the advancing (left) and the receding (right) motion of the ground wire when the power supply is turned off. (c) Close-up of the air-water interface over the ground wire for advancing (left) and receding (right) motion. The contact angles in the advancing and the receding phases of the three-phase contact line formed over the wire were measured to be 78 ± 3° and 64 ± 3°, respectively.

II. EXPERIMENT APPARATUS

The experiment setup developed in the present work is schematically shown in Fig. 1(a). An aqueous solution of 0.1 M KCl in distilled deionized water is prepared. A liquid drop, $6.5 \pm 0.5\ \mu$l in volume, is placed over the chosen surface using a micropipette. Experiments are performed at a controlled room temperature of $\sim 20 \pm 0.4$ °C. The small amount of salt addition does not change the thermophysical property of the water droplet. Specifically, density is 998 kg/m^3, viscosity 1mPa s, and surface tension coefficient in air is 0.072 N/m. The dielectric layer of PDMS having a relative permittivity of 2.76 and dielectric thickness of $\sim 9.4\ \mu$m is coated onto indium-tin-oxide (ITO)-coated glass. ITO coating is connected to the positive terminal of the DC power supply. The copper wire of 0.07-mm diameter is inserted inside the drop that serves as the ground electrode and connected via the negative terminal of the power source. The entire assembly is kept along with a goniometric setup to utilize its horizontal and antivibration bench as well as to keep the ground wire straight. The imaging technique utilizes a high-speed camera, Photron-FASTCAM SA-3 with a frame rate of 7500 frames per second (fps), carefully aligned to record the spreading process. A 200-mm Nikon zoom lens is used to magnify the droplet. In selected experiments, the frame rate was 6000 fps to enable a longer video. Electrowetting experiments have been conducted with a FluoroPel-coated hydrophobic surface as well as a bare PDMS surface.

The PDMS coating is prepared with its base material (liquid PDMS) and the curing agent in a 10:1 ratio. After degasification, it is poured onto the ITO-coated glass in a spin coater. First, a ramp of 500 rpm is set for 10 s, followed by 20 s of rotation at this speed. The second ramp up to 3000 rpm lasts $\sim$30 s and is held constant for 360 s. The ITO-coated glass with a further coating of PDMS is placed in an oven for 1 h at 100 °C. Using an optical profilometer, the resulting coating thickness was found to be $\sim 9.4\ \mu$m. The coating procedure of FluoroPel 1601V on the PDMS is discussed elsewhere [34]. The Field Emission Scanning Electron Microscope images of the textured surfaces are included in the Supplemental Material, Fig. S1 [36]. Ahead of the electrowetting experiment, the substrate thus prepared is cleansed using ethanol.

Voltage is turned on after ensuring that flow disturbances within the drop have subsided. Specifically, velocities are set up during placement of the drop over the surface by the pipette and insertion of the ground wire. The latter alters the interfacial shape of the drop itself at equilibrium (Video S1–S5 in the Supplemental Material [36]). Figure 2(a) shows a time sequence of drop shapes attained in a typical electrowetting experiment when FluoroPel is used as a hydrophobic layer over PDMS. With increase in voltage, a thin film localized at the wire is also to be seen, third row of Fig. 2(a). The wire characterization is carried out during slow insertion and withdrawal process with respect to the drop, thus measuring the advancing and receding contact angles [Fig. 2(b)] with the equilibrium value corresponding to the midphase. Since the ground wire and the liquid droplet are practically at zero voltage, additional spreading arising from electrowetting of the ground wire is neglected.

The time duration of the imaging experiments is $\sim$3 s. The recorded images are analyzed in MATLAB® to retrieve the footprint of the droplet and the interface shape. Here, the Sobel edge-detection algorithm is used. The pixel resolution of the camera in each of the two directions is $\sim 17.5\ \mu$m per pixel. A Savitzky-Golay smoothing filter helps in locating the droplet shape unambiguously. For ease of image analysis, the droplet is divided into the inner ($\sim 200\ \mu$m), intermediate (200–1000 μm), and outer ($>1000\ \mu$m) regions with adequate constraints of continuity. The contact angle is determined by using a quadratic fit of the droplet shape in the inner region. In addition, the contact angle is also measured in the IMAGE J™ software [34]. The two sets of results are consistently within ±3° over the range of experiments studied. However, this approach does not yield the macroscopic dynamic contact angle as discussed at length in Ref. [34]. Since the overall configuration is symmetric, the contact angle reported in the present study is the average of the left and the right contact angles. At voltages below saturation (<200 V), the left and the right contact angles are within ±2° of each other. With further increase in voltage, the difference increases, specifically after the advancing phase. For 263 V, after the first instance of the advancing phase [Fig. 1(c), >10 ms], some measurements show a difference of as high as 5°. These differences may also arise due to localized pinning of the contact line; see Sec. IV C.

The initial equilibrium contact angles of a conducting water droplet on bare PDMS and PDMS coated with FluoroPel are $106 \pm 2^\circ$ and $114 \pm 2^\circ$, respectively, as discussed in Ref. [34]. The CA measurements reported in Fig. 1(b) at higher voltages have been recorded under steady-state conditions. To prevent secondary effects such as film formation and evaporation, it was found important to place a liquid drop on a fresh surface for each data point ahead of applying the required voltage.

Uncertainty in measurements is discussed in terms of the estimated parameters of the contact angle model in Sec. III D.

III. NUMERICAL SIMULATION

A. Numerical methodology

Spreading of a conducting water drop over a hydrophobic substrate is simulated using COMSOL MULTIPHYSICS®, a finite-element solver. A moving mesh module in two-phase flow that utilizes the arbitrary Lagrangian-Eulerian (ALE) formulation has been adopted for tracking the gas-liquid interface. With this approach, interfacial waves as well as the three-phase contact line motion over the substrate and the ground wire are resolved. The governing equations are solved for velocities and pressure in air and water in the geometry shown in Fig. 3. Under isothermal and incompressible conditions for a Newtonian fluid, the equations of motion in the coordinate free form are given as

$$\nabla \cdot \mathbf{u} = 0, \tag{2}$$

$$\rho\left(\frac{\partial \mathbf{u}}{\partial t} + (\mathbf{u}\cdot\nabla)\mathbf{u}\right) = \nabla\cdot\mathbf{T} + \rho\mathbf{g}, \tag{3}$$

where $\mathbf{T} = -p\mathbf{I} + \mu(\nabla\mathbf{u} + \nabla\mathbf{u}^T)$. Further, $\mathbf{u}$ represents the velocity vector, ρ is density, and p is the pressure field. At the gas-liquid interface, immiscibility conditions are expressed as

$$\|\mathbf{u}\| = 0, \tag{4}$$

$$\|\mathbf{T}\|\cdot\mathbf{n} = \mathbf{f}_{st}, \tag{5}$$

$$\mathbf{u}_{\text{mesh}}\cdot\mathbf{n} = \mathbf{u}_1\cdot\mathbf{n}. \tag{6}$$

In Eqs. (4) and (5), $\|\cdot\|$ represents the jump condition at the interface and $\mathbf{n}$ is the unit normal at the interface drawn outward from the water droplet. Here, $\mathbf{f}_{st} = \gamma(\nabla_S\cdot\mathbf{n})\mathbf{n} - \nabla_S\gamma$ is the force arising from surface tension wherein $\nabla_S = (\mathbf{I} - \mathbf{n}\mathbf{n}^T)\nabla$ denotes the surface gradient operator; for isothermal conditions, the coefficient of surface tension is a constant and $\nabla_S\gamma = 0$. Further, subscript 1 represents the water phase and 2 is air. Including viscous terms, the normal and tangential components of the stress continuity equation [Eq. (5)] at the droplet-air interface can be stated in expanded form as

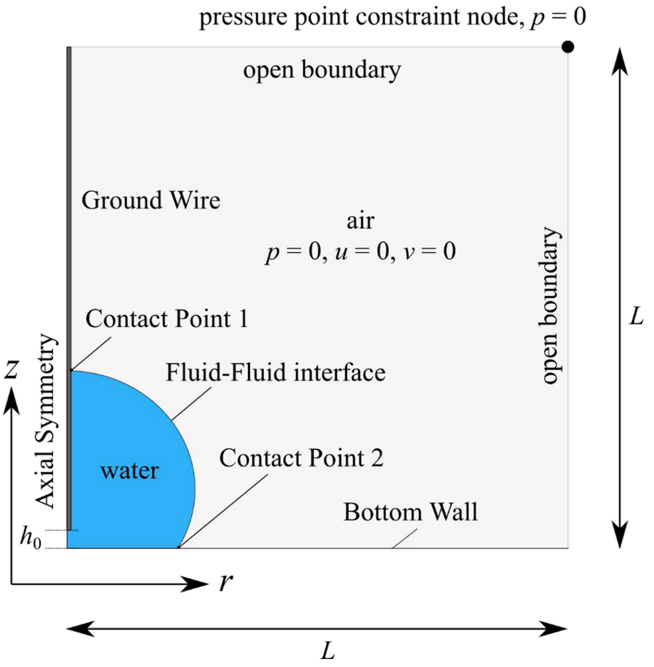

FIG. 3. Initial and boundary conditions in the numerical simulation of drop spreading in an electric field. The bottom wall is a plane above the FluoroPel coating. The distance h_0 (=0.13 mm) in simulations is matched with experiments.

$$\mathbf{n}\cdot([-p\mathbf{I} + \mu(\nabla\mathbf{u} + \nabla\mathbf{u}^T)]_2\cdot\mathbf{n} - [-p\mathbf{I} + \mu(\nabla\mathbf{u} + \nabla\mathbf{u}^T)]_1\cdot\mathbf{n}) = \gamma(\nabla_S\cdot\mathbf{n}), \tag{7}$$

$$\mathbf{t}\cdot([-p\mathbf{I} + \mu(\nabla\mathbf{u} + \nabla\mathbf{u}^T)]_2\cdot\mathbf{n} - [-p\mathbf{I} + \mu(\nabla\mathbf{u} + \nabla\mathbf{u}^T)]_1\cdot\mathbf{n}) = 0. \tag{8}$$

Under equilibrium conditions, velocity components are zero; pressure includes the gravitational contribution and Eq. (7) reduces to the Young-Laplace equation with the drop shape as the unknown. For initial conditions, velocity components are zero and a zero reference pressure is included at the pressure-point constraint node (Fig. 3). The Navier slip-boundary condition is used at the ground wire as well as the boundary above the FluoroPel coating over the PDMS. The slip length is specified as half of the minimum element length and is on the order of a few micrometers, diminishing further with grid refinement [11]. Experiments suggest that the slip length should fall in the nm-μm scale [37]. Such small values cannot be resolved readily on a finite-element grid. Instead, by connecting slip length to element size [11], simulations are shown to be both grid- and slip-length independent with increasing grid resolution (Sec. III C). The computational domain is axisymmetric, with the outer radius and height taken as five times the radius of the droplet defined by the spherical cap approximation. The far-field surfaces are stipulated to be open boundaries. The contact angle models, discussed in Sec. III B, are specified at the contact points "1" and "2" on the ground wire and the lower wall, respectively (Fig. 3). On the axis of symmetry ($r = 0$), normal velocities and tangential stresses reduce to zero. Further, to match experiments, the ground wire is immersed in the drop to a distance of 0.13 mm from the lower surface ($z = 0$).

In the above formulation [Eqs. (2)–(8)] for an axisymmetric geometry, electrowetting is introduced mainly as a change in the contact angle (Sec. III B). Contact angle models for hydrophobic surfaces can be extended to account for electrowetting using the Young-Lippmann equation up to the point of saturation. The applicability of the contact angle model beyond saturation as well as on surfaces with hysteresis is the goal of the present work and discussed in Sec. IV A.

In an ALE simulation, triangular elements in the bulk of the domain deform to accommodate the interface movement. The method proposed in Ref. [38] is utilized for smoothly deforming the mesh while following the boundary constraints; the stiffness parameter is set as 10 for smoothing. Grid independence and validation studies for hydrophobic surfaces before contact angle saturation are presented in Sec. III C.

B. Contact angle model

In the presaturation regime, the equilibrium contact angle closely follows the Young-Lippmann equation and the instantaneous contact angle model can be written as [34]

$$\theta_i = \operatorname{acos}\left[\cos\theta_{\mathrm{YL}} - \frac{\xi \mathrm{Ca}}{\mu} - C_{\mathrm{pin}}\frac{\tanh(C \times \mathrm{Ca})}{\gamma}\right]. \qquad (9)$$

Post saturation, the Young-Lippmann angle is replaced by θ_f in Eq. (9), namely the equilibrium contact angle as recorded in the present set of experiments [Fig. 1(b)]. This approach is further discussed in Sec. IV A. For hysteretic surfaces, the pinning coefficient C_{pin} is greater than zero and the equilibrium contact angle departs from the presaturation value of Young-Lippmann [Eq. (1)], and θ_f beyond the saturation limit. For uniformity in treatment, however, angle θ_f is consistently used in Eq. (9) in place of θ_{YL}, pre- and postsaturation, with the voltage-dependent equilibrium contact angle determined from experiments, as in Fig. 1(b). In Eq. (9), Ca is the capillary number defined in terms of contact line velocity (u_{cl}), dynamic viscosity of the liquid droplet (μ), and the coefficient of interfacial tension as $\mathrm{Ca} = \mu u_{cl}/\gamma$. Further, ξ is the contact line friction coefficient and C is a smoothing parameter. The pining coefficient is defined as [34]

$$\begin{aligned} u_{cl} > 0, \quad C_{\mathrm{pin}} &= \gamma(\cos\theta_f - \cos\theta_a) \quad \text{and} \quad u_{cl} < 0, \\ C_{\mathrm{pin}} &= \gamma(\cos\theta_r - \cos\theta_f). \end{aligned}$$

For $u_{cl} = 0$, the pinning coefficient reduces to zero. The selection criteria for the parameters appearing in Eq. (9) are described in Ref. [34]. Specifically, the advancing and the receding contact angles are calculated based on the local pinning of the contact line, as discussed in Sec. III C, and Sec. IV A. This approach is applicable for steady as well as unsteady contact line motion.

In the numerical simulation, Eq. (9) is adopted as the contact angle boundary condition at "contact point 2" of the lower wall in Fig. 3, with the Young-Lippmann contact angle replaced by the measured equilibrium contact angle. The liquid movement over the ground wire is visible during the receding phase; however, it is mostly small. Hence, at "contact point 1" of the ground wire, Fig. 3, the simplified contact angle model is given as

$$\theta_w = \operatorname{acos}\left[\cos\theta_{ew} - (C_{\mathrm{pin}})_w\frac{\tanh(C_w \times (\mathrm{Ca})_w)}{\gamma}\right]. \qquad (10)$$

The symbols in Eq. (10) have their usual meanings, with subscript w representing the wire and θ_{ew} the intrinsic equilibrium contact angle of the wire surface. Equation (10) is similar to Eq. (9) without the contact line frictional losses. The simplification follows from the small wire diameter where pixel resolution is low and the uncertainty in the measurement of the instantaneous contact angle is large. At later times, a thin film was formed over the wire that invalidated the contact angle treatment. Determination of parameters of Eq. (10) is based on the advancing and receding contact angles over the ground wire as described in Sec. II. In contrast, the equilibrium CA of the droplet at the ground wire (θ_{ew}, Table II) is measured under electrostatic actuation at longer times and after the oscillations have visibly damped.

C. Validation of numerical simulation

The numerical methodology adopted in the present work has been validated against experiments reported in the literature [9,12] and presented in Fig. 4. The simulation parameters used in the contact angle model are summarized in Table I. Figure 4 jointly shows the grid independence of the simulation with the increasing number of cells. The match of simulations with experiments is seen to be quite good, both for 60 V [Fig. 4(a)] and >60 V [Fig. 4(b)]. For Fig. 4(a), the information related to surface hysteresis in experiments is not provided and is a source of uncertainty. For the present comparison, the hysteresis data are estimated from Ref. [11] since the experimental conditions are similar in Fig. 4(a). For Fig. 4(b), the hysteresis data are specified in the literature [9]. In the contact angle model [Eq. (9)], the contact line friction coefficient ξ has to be specified for the chosen surface. It is estimated by fitting the instantaneous contact angle data against the capillary number in appropriate experiments as described in Ref. [34]. For Figs. 4(a) and 4(b), the friction coefficient is listed in Table I. Its value for the FluoroPel surface at 197 V is discussed later [Fig. 5(a)] and given in Table I. The extracted value of ξ is surface specific and shows weak dependence on voltage for the given experimental conditions and hydrophobic coating. Below saturation, past work shows that contact line friction decreases with increasing voltage [39,40]. In contrast, it is shown in Ref. [13] that the friction coefficient remains constant for up to 700 V and decreases beyond. For Parylene-C used in Ref. [9] [Fig. 4(b)], Table I shows that the friction coefficient is practically independent of the applied voltage over 80–120 V and decreases slightly for 140 V in the advancing phase. Changes arising from one hydrophobic surface to another can be seen in Table I.

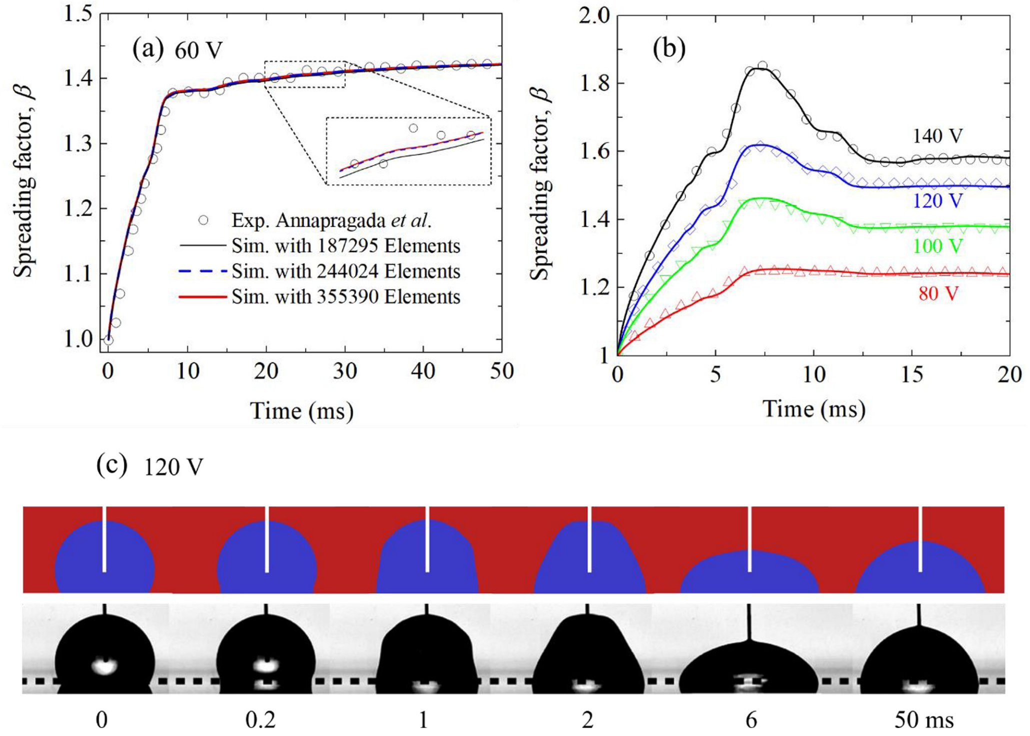

FIG. 4. Validation of numerical simulation with experiments for spreading of a conducting water droplet of 5-μl volume. In (a) and (b), experimental data are represented by symbols, while solid lines represent the numerical simulation of the present work. The hydrophobic coating in (a) is Teflon [12], and for (b) and (c), it is Parylene-C [9]. For (a), the ground-wire diameter is 125 μm, whereas for (b), it is 80 μm. In (c), drop shapes attained at 120 V are presented with the first row being simulations and the second row, experiments. Parameters related to the contact angle model are listed in Table I. Experimental images in (c) have been reprinted with permission from Ref. [9].

Characterization of the ground wire is not available in the literature [9,12]. Hence, for Eq. (10), Table II reports parameters extracted from the present sets of experiments. The simulations in Fig. 4(b) are barely sensitive to the ground-wire properties at low voltages but show a slight dependence at higher voltages when droplet oscillations are pronounced.

As discussed in Ref. [34], hysteresis relates to the dynamic nature of droplet spreading and cannot be determined from quasistatic experiments. Section S3 of Supplemental Material [36] discusses optimization for parameters when hysteresis as well as the friction coefficient is not known. For a Parylene-C surface [Fig. 4(b)], hysteresis in Table I is ∼12° for all voltages, whereas the static hysteresis in Ref. [9] is stated to be 10 ± 3°. For 60 V [Fig. 4(a)], hysteresis for the Teflon surface in Table I is 14°, and the reported value in Ref. [11] is 16°. Hence, in view of the interpretation of hysteresis as a dynamic property of drop spreading over the surface, the

TABLE I. Numerical parameters used for validation of electrowetting simulations.

θ_f (°)	θ_a(°)	θ_r(°)	C_{pin}(N/m) $u_{cl} > 0$	C_{pin}(N/m) $u_{cl} < 0$	ξ(Pa s) $u_{cl} \geqslant 0$	ξ (Pa s) $u_{cl} < 0$	C ($\times 10^4$)
Figure 4(a), 60 V, Teflon [12]							
87	99	85	0.0148	0.0025	0.13	0.1	1.1
Figure 4(b), 80 V, Parylene-C [9]							
100.8	107	95	0.0075	0.0072	0.05	0.05	1.1
Figure 4(b), 100 V, Parylene-C [9]							
88	94	83.5	0.0074	0.0056	0.05	0.05	1.1
Figure 4(b) and Fig. 4(c) at 120 V, Parylene-C [9]							
78	84.4	72	0.0079	0.0072	0.05	0.05	1.1
Figure 4(b), 140 V, Parylene-C [9]							
73	74	63	0.0011	0.0116	0.02	0.05	1.1
Figure 5, 197 V, FluoroPel (present)							
68.8	70	58	0.0013	0.0122	0.04	0.04	1.1

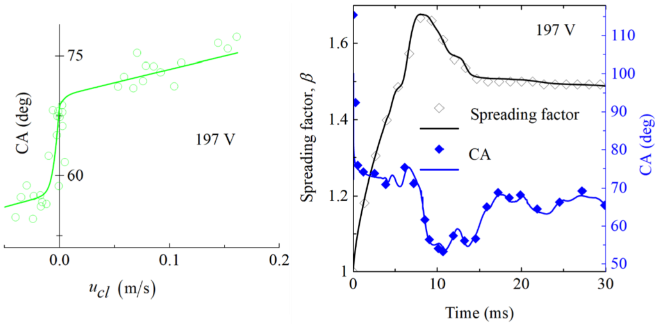

FIG. 5. (a) Instantaneous CA distribution plotted as a function of the instantaneous contact line velocity; symbols represent experimental data, and the solid line represents Eq. (9) in the presaturation regime. (b) Comparison of experimental (symbols) and simulation (solid lines) data for spreading factor and the contact angle as a function of time. Actuation voltage is 197 V. Uncertainty in the CA measurement from imaging is ±2° and ±0.02 mm for the footprint radius.

values presented in Table I differ slightly from those in the literature [9,11].

Simulation is reported in the present work with a total of 244 024 triangular elements while resolving droplet movement over the ground wire [Fig. 4(a)]. The spreading data obtained were seen to be invariant to the choice of the number of elements varied over 187 295 to 355 390, the peak footprint and droplet height differences being on the scale of a few micrometers. Further, for the chosen grid (244 024 triangular elements), the slip length is below ∼1 μm. With further grid refinement, the slip length falls below ∼0.5 μm. Grid-independence studies simultaneously show the adequacy of the chosen grid along with a near independence from the specification of the slip length.

D. Validation of simulations with experiments in the presaturation regime

Selected experiments have been carried out in the present work in the presaturation regime for an applied voltage of 197 V. The parameters used for the contact angle model are extracted from experimentally determined contact angle–contact line velocity data shown in Fig. 5(a). These are listed in Table I, last row marked FluoroPel. The comparison of simulations with experiments is shown in Fig. 5(b), and the agreement is seen to be quite good. The close match in Fig. 5(b) validates the experimental procedure as well as the choice of Eq. (9) as the contact angle model in simulations, particularly in the presaturation regime. A similar match was seen at other voltages for the parameters specified in Table S3 [36]. Below saturation, θ_f is found to be close to the Young-Lippmann value, the uncertainty band being $\theta_{\mathrm{YL}} \pm 3^\circ$ while the contact angle hysteresis is $10 \pm 2^\circ$. The friction coefficient falls in the range of 0.038 ± 0.002 Pa s while the smoothing parameter is a constant at 1.1×10^4 for the range of parameters studied. Beyond saturation, these parameters differ in the advancing and receding phases, as discussed in Sec. IV A.

TABLE II. Numerical parameters for the ground wire in electrowetting simulations.

θ_{ew} (°)	θ_{aw}(°)	θ_{rw}(°)	$(C_{\text{pin}})_w$(N/m) $u_{cl} > 0$	$(C_{\text{pin}})_w$ (N/m) $u_{cl} < 0$	C_w ($\times 10^4$)
72	78	61	0.0073	0.0127	1.1

IV. RESULTS AND DISCUSSION

Droplet spreading on a hydrophobic surface has been extensively studied in the literature [41,42] and more recently by the authors [34] where a contact angle model was proposed. The present study aims at understanding the spreading dynamics under electrowetting conditions. Special interest is directed toward spreading in the post-contact angle saturation regime. In the first subsection, the discussion relates to a PDMS surface coated with FluoroPel in which experimentally recorded spreading details, CA variation, and drop shapes are presented in relation to numerical simulation. The second subsection includes the effect of the position of ground wire on interface deformation. Limiting cases of the ground wire inserted within the drop placed over the FluoroPel-coated surface and the ground wire kept 40 μm above the apex of the drop placed over bare PDMS are compared. The third subsection compares experimental data at a high voltage beyond saturation for FluoroPel-coated and PDMS surfaces over a longer duration.

A. Drop spreading over a FluoroPel-coated surface

Figure 6 shows the experimentally recorded contact angle variation of a conducting water drop over a FluoroPel-coated surface as a function of time for the first 50 ms. Actuation voltages of 175, 197, and 263 V are considered for the present discussion with 200 V being the contact angle saturation limit. After the actuation of the electric field, the contact angle decreases within 1 ms. Subsequent spreading is distinct and voltage dependent; also see Fig. 1(c) for voltage-dependent spreading of the drop. The sudden reduction in the contact angle is the origin of a capillary wave that strengthens with increasing voltage, in confirmation of the work of Vo *et al.* [32].

In the initial stages, Fig. 6 shows three broad trends for the voltages studied. These relate to small contact angle changes when the drop advances or recedes over the surface, a pinned constant line when the contact angle rapidly increases or decrease with time, and a long-term relaxation phase. The third phase is increasingly delayed at higher voltages. The changes in the contact angle along with spreading and height oscillations are connected to the flow field within the drop that, in turn, arises from the capillary wave initiated over the gas-liquid interface.

At 175 V, small changes in contact angle prevail during the time intervals of 1–5 and 10–15 ms during which the drop spreads and retracts, respectively, as seen in the spreading ratio plot of Fig. 1(c). The pinning regimes are short-lived and decrease in duration at higher voltages. Momentary pinning effects can also be seen within the advancing and receding phases of the drops. Even at low voltages,

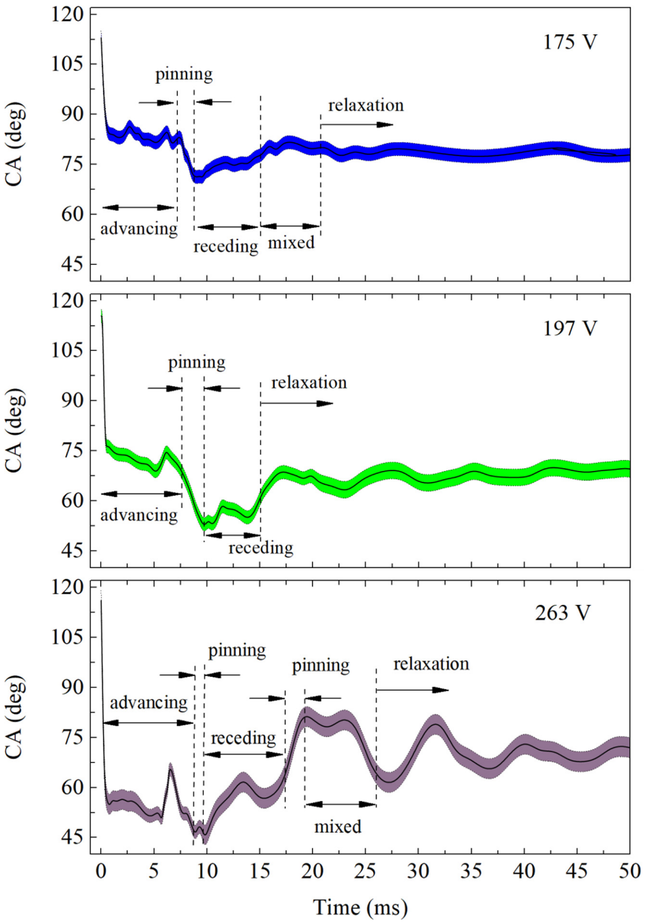

FIG. 6. Experimentally determined instantaneous contact angle (CA) variation with time for a conducting water drop actuated at 175, 197, and 263 V. The PDMS dielectric layer is coated with FluoroPel. The shaded regions in the graphs shown represent the uncertainty.

small-scale oscillations persist in the long-term relaxation regime (>20 ms for 175 and 197 V). For an actuation voltage (263 V) greater than the saturation value, the spreading-pinning cycles (called "mixed" in Fig. 6) persist for a longer time and large-scale oscillations are initiated in the relaxation phase as well. These spreading characteristics of the drop including long-term oscillations connect directly with the initial formation of a capillary wave [see Fig. 2(a)]. Hence, a match between simulations and experiments requires that the interfacial capillary wave be resolved with care. In addition, reproducing experimental data will require setting up an appropriate contact angle model.

The complexities in contact angle variation with time may also arise because of the electrical detachment of the ground wire with the droplet [43] during spreading. However, this possibility is not expected to be significant in the present discussion since the ground wire is initially located well within the drop.

Figure 7(a) shows the duration of the first pinning event as a function of the applied voltage. Below saturation, the duration is nearly constant while it progressively decreases with voltage beyond saturation. A constant pinning duration with voltage suggests a predictable advancing-pinning-receding sequence of events that is followed by a long relaxation tail. As the pinning duration decreases, the number of pinning events increases, leading to long-term oscillations. The first column of Fig. 7(b) shows an image sequence of the droplet during the pinned phase with a practically constant footprint radius when a small reduction in contact angle is registered (also see Fig. 6 for 263 V). A slight increase in drop height is to be noted in the form of the wetted film at the ground wire. The second column shows a later time sequence when the changes in contact angle are small while the footprint diameter reduces during the receding phase. The decrease in footprint diameter is initially accommodated by a reduction in height at the axis and later with a peak away from it, while at subsequent frames, the drop height at the axis increases progressively with time. Referring to the postsaturation regime in Fig. 6, it may also be noted that the equilibrium contact angle after relaxation is greater than the value predicted by Eq. (1).

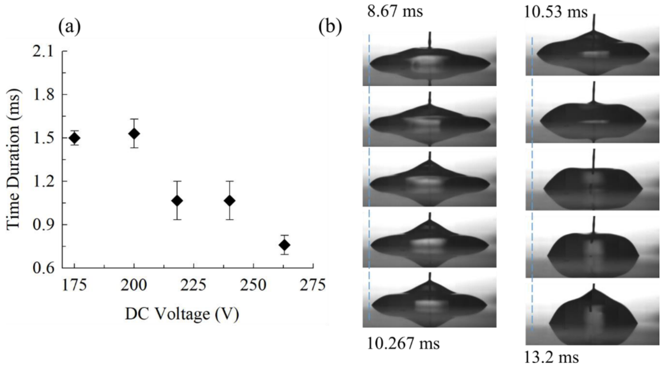

FIG. 7. (a) Time duration of the first instant of pinning with respect to the applied voltage; (b) motion of droplet over the FluoroPel-coated surface close to the first instant of pinning at 263 V. In (b), the first column shows pinned images of the drop before the onset of the receding phase with the time elapsed between successive frames being 0.4 ms. The second column shows the first receding phase with a time separation of 0.67 ms.

For the FluoroPel-coated surface, initial pinning is less likely to relate to the hysteretic features of the physical texture; see Ref. [34] for spreading dynamics under zero voltage conditions. Instead, pinning can be a momentary consequence of the balance between the interfacial capillary wave counteracted by the kinetic energy of the bulk of the fluid. In the long run, both factors diminish owing to viscous effects. At this stage, pinning solely depends upon the nanoscale surface texture and is revealed in the relaxation phase of Fig. 6. Beyond saturation, the two factors are energized and viscous effects are less effective, leading to long-term pinning-spreading-oscillation cycles. In this respect, pinning of the drop over the surface is a metastable state, soon to be destabilized by the available energy components. As expected, oscillation amplitudes increase with the magnitude of the external voltage.

Figure 8 represents the experimentally determined instantaneous contact angle plotted as a function of the contact line velocity for an external voltage of 240 V. The arrows show the spreading details of the drop starting from the initial time instant. In the advancing phase, the instantaneous CA decreases with a reduction in the contact line velocity; however, in the receding phase, the CA distribution shows two

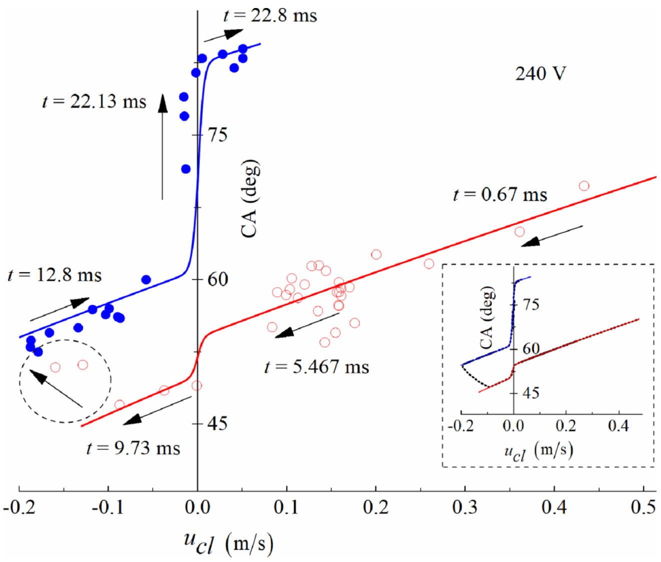

FIG. 8. Contact angle plotted as a function of contact line velocity for the conducting droplet actuated at 240 V over a FluoroPel-coated surface. Symbols show experimental data and the solid line is the contact angle model, Eq. (9). Red line and symbols represent the initial part of the spreading process (<10 ms). Blue represents the spreading behavior after the instant of first pinning. The direction of the arrow illustrates the progress of time for a total of ∼24.13 ms, wherein the time instants stated are associated with the tip of arrow head. Contact angle recovery is initiated in the receding phase when the contact line velocity is negative (dotted circle). The uncertainty associated with the CA measurement is ±3° at 240 V. (Inset) Dotted black line shows contact angle variation with contact line velocity in simulations.

distinct patterns. Soon after the retraction of the contact line (∼9.7 ms), the contact angle functionality with contact line velocity undergoes a transition, as shown by the dashed circle. Thus, the data falling on the red line transform to the blue, and the contact line motion is retarded. Subsequent motion is in conformity with the expectations of the contact angle model. For the postsaturation regime, spreading is possibly impacted by charge trapping, mainly in the receding phase, as described by Li [31]. The reduction in charge availability at the contact line can explain the increase in contact angle initiated in the receding phase.

In Fig. 8, the contact angle model based on pinning and friction [Eq. (9)] matches the experimental behavior of contact angle distribution fairly well except in the region marked by a dashed circle, where there is a jump. The time duration corresponding to this circle is ∼0.8 ms (beyond 9.73 ms), where spreading undergoes the transition from red to blue, and the contact line velocity starts to increase. After the transition, the CA distribution is largely influenced by the contact angle hysteresis, shown as a jump in the increase in contact angle. The magnitude of the jump and the subsequent evolution, primarily marked in blue, depends on the surface properties. After ∼23 ms (beyond the advancing phase in blue), the pinning of the contact line restricts further contact line motion, and the drop oscillates between the maximum and the minimum value of the contact angle. These oscillations are bound by the jumps in the CA distribution. This trend is unique to the postsaturation regime, while below saturation, contact angle changes follow the red curve alone [Fig. 5(a), 197 V].

Prior to saturation, the methodology applied for the evaluation of parameters in Eq. (9) is identical to those used to predict the experimental data of Fig. 5 and discussed earlier in Ref. [34]. Following a similar approach for the postsaturation regime, parameters for the contact angle model are derived from Fig. 8 at an actuation voltage of 240 V. This leads to two distinct contact angle models, one for the red curve and the second for the blue. The form of Eq. (9) is unchanged, except that a unique set of parameters is applicable for each stage. The red line denotes the first phase of spreading. The minimum and maximum contact angles around the pinning phase can be associated with the advancing and receding values. The metastable state (8.53–9.46 ms) shown by the jump in contact angle can be used for the θ_f calculation. Simulation showed that the spreading details were insensitive to the choice of θ_f since other terms in Eq. (9) have a substantive role.

For the blue line in Fig. 8, the advancing and receding contact angles have been adopted from the second instant of pinning (16–19 ms). As per Eq. (9), the equilibrium contact angle is attained by the droplet after long-time relaxation, but the present discussion is restricted to the initial stages (∼50 ms).

The contact line friction coefficient (ξ) and the smoothing parameter (C) in Eq. (9) are derived by curve fitting as in Fig. 8 and are summarized in Table III. These are subsequently used in the simulation of the electrically actuated drop spreading over a FluoroPel-coated surface. The respective sets of parameters for the red and blue lines are fairly independent of voltage though depending on the nature of the surface. However, red-to-blue transition is not predicted in the present approach. The instantaneous contact angle data extracted from a numerical simulation at 240 V are shown as an inset of Fig. 8 as a dotted black line.

Water drop spreading over FluoroPel with a small initial velocity of ∼0.09 m/s has been discussed earlier by the

TABLE III. Numerical parameters used in electrowetting simulations for 240 V.

θ_f (°)	θ_a(°)	θ_r(°)	C_{pin}(N/m) $u_{cl} > 0$	C_{pin}(N/m) $u_{cl} < 0$	ξ(Pa s) $u_{cl} \geqslant 0$	ξ (Pa s) $u_{cl} < 0$	C ($\times 10^4$)
Figure 8 (red); Figs. 9 and 10 at 240 V (up to the peak, ∼10 ms, postsaturation)							
52	54	50	0.002	0.00195	0.036	0.036	1.1
Figure 8 (blue); Figs. 9 and 10 at 240 V (after peak, >10 ms, postsaturation)							
71	82.5	61	0.014	0.0115	0.036	0.036	1.1

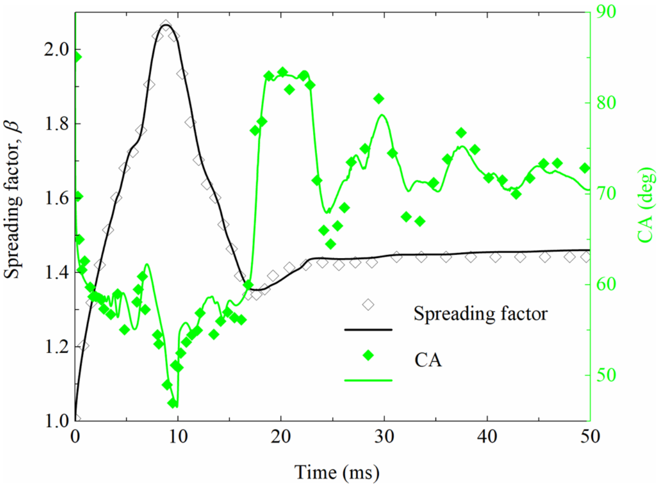

FIG. 9. Spreading factor and contact angle variation with time for a FluoroPel-coated substrate with an actuation voltage of 240 V. Symbols show experimental results while solid lines represent numerical simulation. In experiments, the measurement uncertainty in CA is ±3º. For the spreading factor, uncertainty in footprint measurement is ±0.02 mm. Parameters used in the simulation are summarized in Table III.

authors with a zero actuation voltage. The contact angle hysteresis accompanying the unsteady motion of the contact line was ∼13.3º. In electrowetting experiments for 197 V (below saturation), the hysteresis is ∼12º. Beyond saturation, a higher hysteresis (∼21.5º) is to be seen in the receding phase (Fig. 8, blue curve). In the advancing phase, the friction coefficients for 0, 197, and 240 V are quite close; however, for 0 V in the receding phase, it has a higher value (0.08 Pa s) compared to 197 and 240 V, that are quite close to each other. For 197 and 240 V, the smoothing parameter in Eq. (9) is close to its value at 0 V.

Figure 9 compares numerical simulation with imaging experiments for drop spreading in the postsaturation regime. Here, symbols represent experimental data, and the continuous line is from simulations. The match in terms of the spreading factor as well as the instantaneous contact angle is seen to be good. Combining Figs. 5 and 9, it is seen that the match between simulations and experiments is good, both in the pre-and postsaturation regimes. Thus, the comparison is quite favorable in every regime of spreading arising from Fig. 6. As discussed below, simulations also reveal late-time oscillations for a stationary contact line, the metastable state attained at the peak of the spreading factor, and the advancing and the receding contact line motions, in accordance with experiments.

Figure 10 compares simulated drop shapes with experimental images for an actuation voltage of 240 V (see experimental Video S2 in the Supplemental Material [36]). The two sets of images show a good level of agreement. However, there is a small mismatch at intermediate times (∼9.06 ms) at the ground wire. The reason could be the

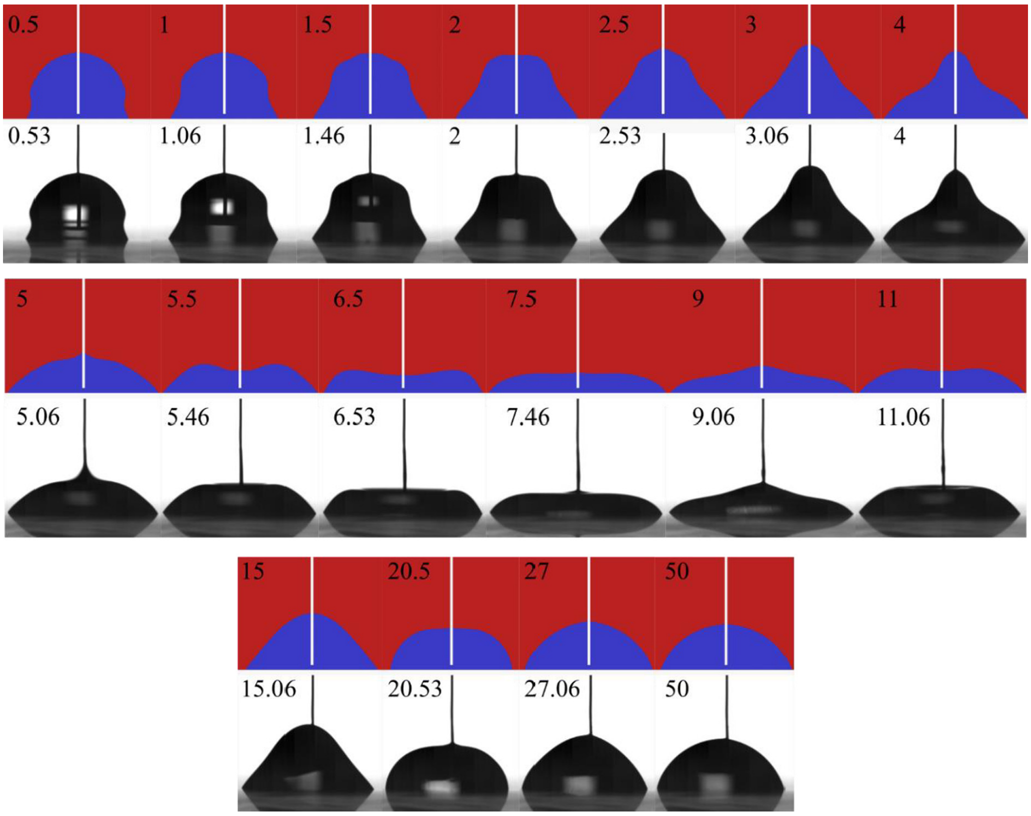

FIG. 10. Experimental images (black against a white background) and simulated data (blue against red) of instantaneous shapes attained by a liquid drop at an actuation voltage of 240 V. Numbers accompanying the images are time instants in ms. While spreading is over a FluoroPel-coated surface, the ground wire of diameter 0.07 mm in simulations has wetting characteristics.

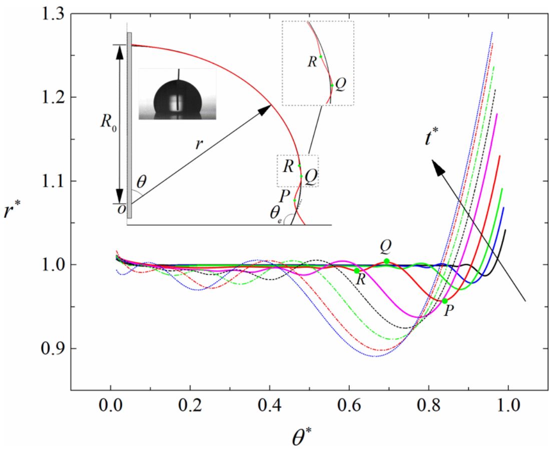

FIG. 11. Simulation of capillary wave propagation over the water-air interface at an applied voltage of 263 V when the ground wire is immersed in the drop. Arrow direction indicates time marching ($t^* = t/\tau$, where $\tau = \sqrt{\rho R_0^3/\gamma}$); further, $r^* = r/R_0$, and $\theta^* = \theta/\theta_e$. Time instants considered are $t^* = 0.0186$, 0.037, 0.056, 0.093, 0.15, 0.186, 0.223, 0.26, and 0.279, following the arrow shown. Inset (monochrome image) represents the initial experimental condition where the drop is placed over FluoroPel-coated surface. Its equivalent image (right half of the inset) in simulation is represented by a black line. Simulation parameters in Eq. (9) for initial spreading ($t \leqslant 1.5$ ms) are $\xi = 0.036$ Pa s, $\theta_f = 49.5^\circ$, $C_{\text{pin}} = 0.00096$ N/m, and $C = 1.1 \times 10^4$; see Sec. S4 of Supplemental Material [36] for spreading factor and contact angle variation with time.

formation of a precursor film over the ground wire in experiments, while simulations treat the wire as dry at all times. The film may form during liquid advancement over the wire following the advancing phase over the substrate. The presence of the film is then felt when drop motion is pinned first and is followed by a receding motion. In simulations, the contact angle model is applied at the substrate and the ground wire without reference to the film. At later times, flow transitions such as retraction as well as recovery of contact angle have taken place, and experiments show a slight loss of symmetry (∼15 ms). This trend is not seen in the simulation where an axisymmetric approximation has been adopted. However, after 20.53 ms, the two halves of the water-air interface appear identical relative to the ground wire, and symmetry is restored. At much higher voltages, the ground wire plays a disruptive role in breaking symmetry, as discussed in Sec. IV C.

Figure 11 shows numerically simulated interfacial deformation as a function of time when the ground wire is immersed in the drop. Early-time instants are considered to clearly reveal drop deformation. A polar plot representation is shown in dimensionless coordinates, where θ^* represents the angular position and r^* is the radial position of the interface indicating the wave amplitude; see the caption of Fig. 11 for their definitions. The polar plot qualitatively reveals wave propagation over the gas-liquid interface with an increase in time. Since the wave amplitude damps with time [32], Fig. 11 shows time instants for which $t^* < 1$, revealing $\sqrt{\gamma/\rho R_0}$ as an appropriate inertia-capillary velocity scale. The initial contact line velocity arising from electrical actuation should be greater than the inertia-capillary velocity scale for a sustained capillary wave. At 263 V considered in Fig. 11, the contact line moves rapidly, whereas the amplitudes of selected points, such as Q and R, follow the initial curvature of the undeformed liquid drop. Experiment images [top row of Fig. 2(a)] show that the second negative curvature at point R is not visible during early times. With time advancement, the amplitude of the capillary wave increases and propagates toward the apex. At the tail of the wave ($\theta^* \sim 0.014$), the wetting condition of the ground wire damps the wave amplitude. Examining the time instants considered in Fig. 11, it is seen that surface deformation progresses rapidly along with the interface with the ground wire serving as a pinned end ($t^* \leqslant 0.223$). The correlated motion of points such as P, Q, and R confirms a wavelike behavior of the interface during spreading.

B. Effect of the axial position of the ground wire

In the previous section, the ground wire was inserted deep within the drop, covering ∼94% of the initial drop height. For a wire whose surface has wetting characteristics, Fig. 10 shows that the drop moves over the wire and has an impact on flow distribution and interface deformation. In addition, wire position alters electrohydrodynamic forces, specifically Maxwell's stresses, that are responsible for electrowetting. Previously, Baret *et al.* [43] studied oscillations of an aqueous drop placed over a hydrophobic coating in an oil environment. The ground wire was kept inside the drop at a fixed height from the substrate. The authors reported stable drop oscillations between the attached and the detached condition of the wire with respect to the drop. At the instant of detachment, Maxwell's stresses reduce to zero at the contact line, and the macroscopic contact angle reduces, under limiting conditions, to Young's contact angle. Thus, wire position plays an important role in the dynamics of electrowetting. In the present section, interface deformation in the form of capillary waves is discussed for a wire that has a separation of 40 μm from the apex of the drop (Fig. 12). It is further compared with Figs. 2 and 11 at 263 V where the wire is initially immersed in the drop. Since the surface hysteresis does not play a role in the initial time instants, experiments in Fig. 12 have been carried out over a PDMS surface.

For an initially detached ground wire (Fig. 12), electric-field actuation causes first a slight change in the drop shape. Electrostatic forces lead to the droplet just touching the ground wire, as shown in Fig. 12(a). For a good conductor, the charge relaxation time ($\varepsilon\varepsilon_0/\sigma$) of ions inside the drop is small (∼μs) as compared to the spreading timescale ($\rho\ell^2/\mu$) of fluid motion [44]. Thus, following contact between the apex of the drop and the wire, spreading is initiated at the substrate [see Fig. 12(b)] before 0.5 ms. Spreading can also be seen in Fig. 12(c) from 0 to 0.167 ms. Electrostatic attraction at the apex of the drop does not last long, and at 0.33 ms in Fig. 12(c), the wire gets detached. There is a time lag of one frame between the detached condition at the ground wire and the movement at the substrate [Figs. 12(b) and 12(c)], the time difference between the two frames being 0.167 ms. Postdetachment, contact angle relaxation is slow and is expected to depend on the uniformity of the dielectric surface [43]. In the present study, the contact line is pinned after wire detachment, and the contact angle relaxes in a duration on the order of

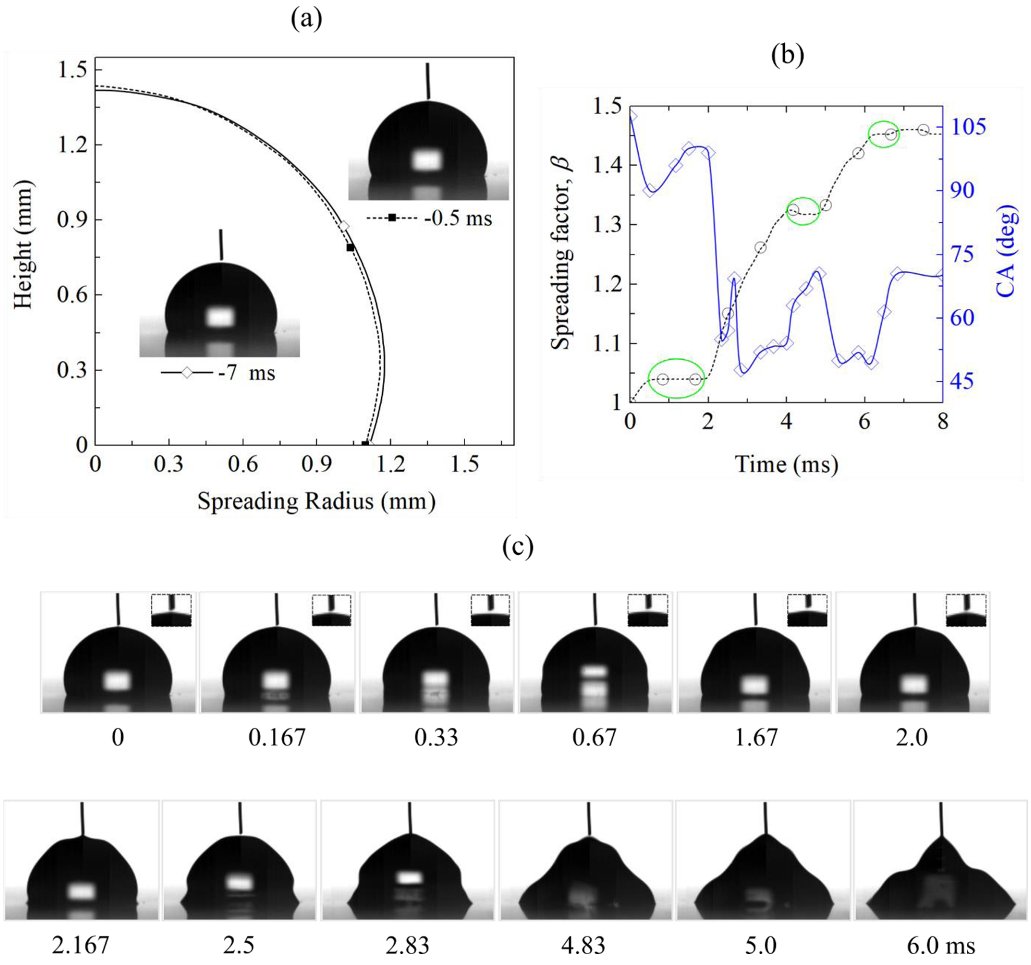

FIG. 12. Experimentally determined capillary wave propagation for a noncontacting ground wire when the drop is actuated with 268 V over PDMS that serves as the dielectric as well as hydrophobic coating. The initial distance between the ground wire and the top of the apex of the drop is ~0.04 mm. (a) Drop shapes recorded before −7 and −0.5 ms of electrostatic actuation are shown; (b) variation of spreading factor (black line with open circles) and contact angle (blue line with open diamonds) with time; and (c) experimental images of the evolution of the capillary wave during attached and detached condition of the droplet with the ground wire. In the top row, each frame is provided with inset indicating possible contact of the wire and apex of the drop. The measurement error in footprint radius using pixel count is within ±0.02 mm, and uncertainty in contact angle measurement is ±3°.

milliseconds until the drop touches the wire [Fig. 12(b)]. The frequent contact and loss of contact of the drop with the wire in the early stages affects charge distribution, leading to lower spreading relative to the FluoroPel-coated surface. This is a point of difference from Fig. 11, where the wire is consistently immersed in the drop. Beyond 0.167 ms, the wire is detached from the drop; the original contact angle-related curvature is regained until about 2 ms. This regime, encircled in green in Fig. 12(b), shows a near-constant spreading factor.

Early spreading [Fig. 12(c), from 0.67 to 2.167 ms] also supports a capillary wave at the interface that alters curvature from negative when the drop attaches to the wire to positive when the two are detached. After 2.0 ms in Fig. 12(c), interface curvature causes the droplet-wire contact, and spreading equivalent to Fig. 11 commences. Specifically, the contact angle decreases, followed by an increase in the spreading factor.

There is a point of difference between the capillary wave propagation for immersed and detached ground wires. In the latter, the drop intermittently touches the wire, causing the interface deformation to be a superposition of multiple capillary waves independently initiated at various time instants; see Fig. 12(c) from 2.83 to 6 ms and the multimedia view (Video S4 [36]). Referring to the green circles in Fig. 12(b), spreading is arrested under detached conditions while advancing, and receding motions are realized when the two are in contact.

C. Spreading over a FluoroPel-coated surface compared with bare PDMS in the postsaturation regime

At high voltages, internal hydrodynamics in the drop becomes strong; the ground wire is repositioned, leading to three dimensionality. In this context, experimental results of spreading at 263 and 268 V are discussed for FluoroPel [Fig. 13(a)] and bare PDMS [Fig. 13(b)]. See Video S3 for FluoroPel and Video S5 for PDMS in the Supplemental Material [36]. Both surfaces have spatially uniform microstructure down to a nanoscale resolution (Fig. S1 [36]). Further, for PDMS, the contact angle hysteresis is higher [34]. De Gennes [33] described how surface heterogeneity and hysteresis distort the

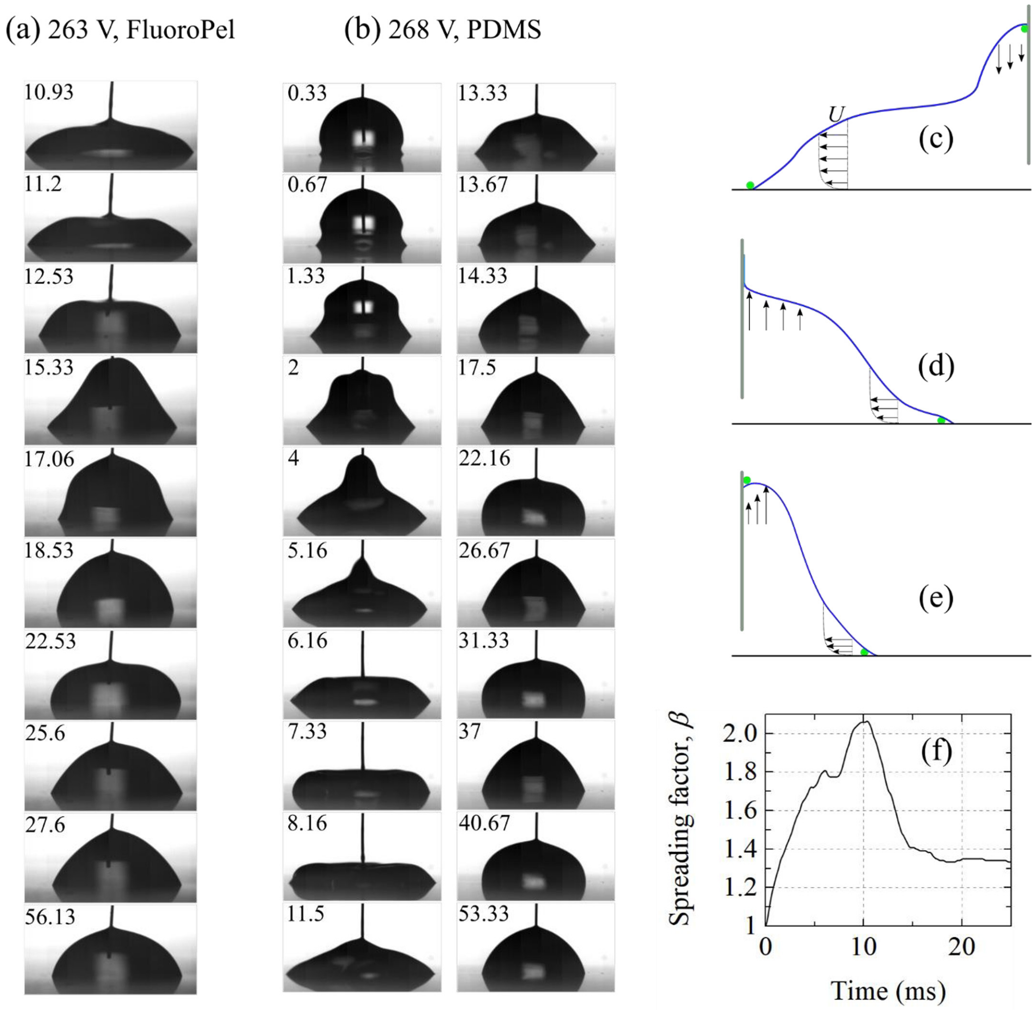

FIG. 13. Experimental images of drop shapes seen on (a) FluoroPel and (b) PDMS for a ground-wire diameter of 70 μm. Parts (c) and (d) are schematic drawings of drop motion in the advancing and receding phases, respectively, while (e) is receding motion after the thin film at the ground wire is crossed. Blue represents the liquid-air interface and the green circle is the energy barrier of the surfaces. Arrows and their length are related to direction and velocity magnitude, respectively. (f) Variation of spreading factor with time for the PDMS substrate when the applied voltage is 268 V; spreading radius has the measurement error of ±0.02 mm.

liquid-gas interface emanating from the contact line, consistent with Video S3 and Video S5.

Figures 13(a) and 13(b) show that the movement of the three-phase contact line and liquid-air interface are quite uneven in space and time. Over FluoroPel, the left and the right contact points move jointly in the advancing phase [Fig. 2(a)]. Fig. 13(c) is a schematic representation of the advancing contact line moving over a hysteretic substrate when it hits the energy barrier, shown as a shaded green circle. Such a blockage is frequent over PDMS, causing a breakdown in axisymmetry.

Figure 13(d) schematically shows the drop receding over the lower substrate. The prewetted film at the ground wire facilitates a smooth motion of the local contact line. At the substrate, contact line motion is intermittent for PDMS, as seen in Fig. 13(b) (13.33 to 17.5 ms). The contact line motion is retarded, and the bulk of the liquid is pushed radially inward. The uneven shape of the interface also creates a pressure imbalance inside the drop. Therefore, an oscillatory phase is initiated [after 17.5 ms, Fig. 13(b)] until the internal disturbances are dissipated by viscosity.

For a low-hysteresis surface such as FluoroPel, the contact line at the wire crosses the prewetted film and meets the dry surface, as shown in Fig. 13(e). The shape of the liquid-gas interface near the wire changes from convex to concave [Fig. 13(a), 11.2–15.33 ms]. However, for PDMS, this change is not seen because of higher hysteresis. The contact line is pinned after ∼17.5 ms [Fig. 13 (b)] at the substrate, and the one at the wire does not reach the dry surface. This trend for PDMS is shown in Fig. 13(f) in terms of the spreading factor.

D. Future prospects

For a FluoroPel-coated surface, numerical results obtained from the proposed contact angle model show good agreement with the experimentally recorded instantaneous drop shapes (Fig. 10) and the spreading factor (Fig. 9). The contact angle model of the present work does not include contact angle transition seen in Fig. 8 in the receding phase. It is related to the charge-trapping phenomenon [31], particularly in the postsaturation regime, and should be considered in future analysis. At higher actuation voltages even beyond saturation (>200 V), the shapes of the contact line and the liquid-vapor interface are seen to be uneven, particularly in the receding phase. At lower voltages ($\leqslant$240 V, Fig. 10), spreading is less distorted, and axisymmetric simulation should be acceptable. For higher voltages (>260 V), 3D simulation is needed to resolve the details of drop shape and motion. This approach will be considered in the future. With a contact angle model such as Eq. (9), the match is expected to be weak for a bare PDMS surface. For PDMS, the surface is hysteretic, namely, it has a distribution of pinning sites that should be known in advance for modeling. Hence, simulations will be specific to a chosen surface.

V. CONCLUSIONS

Spreading of a conducting water droplet over a textured substrate in the presence of a DC electric field has been studied via experiments and simulation. The external voltage, contact angle hysteresis, and the location of the ground wire are independent parameters while the movement and deformation of the liquid-gas interface and the three-phase contact line are subjects of investigation. In simulations, the geometric configuration of spreading is taken to be axisymmetric. A FluoroPel-coated PDMS surface and a bare PDMS surface have been compared. Numerical simulations have been carried out using a contact angle model developed earlier by the authors with corrections arising from the electric field. Simulations show a good agreement with experiments over a wide range of voltages, before and after contact angle saturation. Here, the comparison is in terms of the instantaneous footprint radius, drop shape, and the instantaneous contact angle.

Ahead of the contact angle saturation, experiments show that contact line spreading is symmetric with respect to the position of the ground wire. The instantaneous contact angle increases with contact line velocity when it is positive and decreases for negative contact line velocity, namely, for a retracting contact line. The instantaneous contact angle approaches the equilibrium value given by the Young-Lippmann equation as the liquid drop relaxes to zero velocity. This trend is in conformity with normal spreading seen in both experiments as well as simulations, in the absence of an electric field. Beyond the point of saturation, there is a change in the overall spreading pattern. Contact angle saturation gives rise to two distinct distributions of contact angle with contact line velocity—one before the start of retraction and the second after retraction. It should be contrasted with the presaturation contact angle behavior, where advancing and receding contact angles are strongly correlated with velocity, with additional corrections needed for the pinning sites.

The present study shows that the form of the contact angle model is unchanged with respect to voltage. Below saturation, the model parameters are uniquely determined. Spreading at zero voltage is qualitatively similar to presaturation spreading with a fairly similar set of parameters. Postsaturation spreading is characterized by two sets of model parameters though the form of the model itself is unchanged. With this approach, the experimental trends are correctly reproduced by numerical simulation. In view of the formation of capillary waves, the ground wire plays an important role in spreading. The capillary wave propagated over the liquid-gas interface reaches the ground wire causing substantial shape distortion in this region. The extent of impact of the ground wire depends on its size and wetting properties. Introducing a contact angle model for wire in simulations improves the match with experiments. For a hydrophilic wire, a thin film is formed over it in experiments that, in turn, is not realized in simulations.

For a noncontacting ground wire above the apex of the droplet, distinct structures of the liquid-vapor interface are observed. With a spacing of 40 μm, a crest reaches the apex by a wave that is initiated at the contact line over the substrate. As a result, electrical contact between the droplet and the wire is restored. Multiple events of contact and loss of contact lead to capillary waves of distinct phase and amplitude, and the interface deformation seen is a superposition of these waves.

Beyond saturation, the contact line motion over bare PDMS, a hysteretic substrate, is quite uneven compared to one of low hysteresis (FluoroPel-coated PDMS). The contact line is pinned at specific sites, nucleating unsymmetrical spreading and uneven dynamics of the liquid-vapor interface. The resulting contact line motion is intermittent. It is expected that the parameters of the contact angle model for such surfaces will have to be recovered from 3D simulation that includes the details of surface texture and is a topic for future work.

[1] G. Lippmann, Relation entre les phénomènes électriques et capillaires, Ann. Chim. Phys. **5**, 494 (1875).

[2] F. Mugele and J. C. Baret, Electrowetting: From basics to applications, J. Phys.: Condens. Matter **17**, R705 (2005).

[3] T. B. Jones, On the relationship of dielectrophoresis and electrowetting, Langmuir **18**, 4437 (2002).

[4] T. B. Jones, J. D. Fowler, Y. S. Chang, and C. J. Kim, Frequency-based relationship of electrowetting and dielectrophoretic liquid microactuation, Langmuir **19**, 7646 (2003).

[5] M. Vallet, M. Vallade, and B. Berge, Limiting phenomena for the spreading of water on polymer films by electrowetting, Eur. Phys. J. B **11**, 583 (1999).

[6] K. H. Kang, How electrostatic fields change contact angle in electrowetting, Langmuir **18**, 10318 (2002).

[7] F. Mugele, Fundamental challenges in electrowetting: From equilibrium shapes to contact angle saturation and drop dynamics, Soft Matter **5**, 3377 (2009).

[8] A. I. Drygiannakis, A. G. Papathanasiou, and A. G. Boudouvis, On the connection between dielectric breakdown strength, trapping of charge, and contact angle saturation in electrowetting, Langmuir **25**, 147 (2009).

[9] J. Hong, Y. K. Kim, K. H. Kang, J. M. Oh, and I. S. Kang, Effects of drop size and viscosity on spreading dynamics in DC electrowetting, Langmuir **29**, 9118 (2013).

[10] J. M. Oh, S. H. Ko, and K. H. Kang, Analysis of electrowetting-driven spreading of a drop in air, Phys. Fluids **22**, 032002 (2010).

[11] Y. Lu, A. Sur, C. Pascente, S. Ravi Annapragada, P. Ruchhoeft, and D. Liu, Dynamics of droplet motion induced by electrowetting, Int. J. Heat Mass Transfer **106**, 920 (2017).

[12] S. R. Annapragada, S. Dash, S. V. Garimella, and J. Y. Murthy, Dynamics of droplet motion under electrowetting actuation, Langmuir **27**, 8198 (2011).

[13] C. Decamps and J. De Coninck, Dynamics of spontaneous spreading under electrowetting conditions, Langmuir **16**, 10150 (2000).

[14] J. Kim and M. Kaviany, Electrowetting purged surface condensate in evaporators, Heat Transfer Eng. **31**, 101 (2010).

[15] R. Dey, J. Gilbers, D. Baratian, H. Hoek, D. Van Den Ende, and F. Mugele, Controlling shedding characteristics of condensate drops using electrowetting, Appl. Phys. Lett. **113**, 243703 (2018).

[16] N. Miljkovic, D. J. Preston, R. Enright, and E. N. Wang, Electric-field-enhanced condensation on superhydrophobic nanostructured surfaces, ACS Nano **7**, 11043 (2013).

[17] R. Blossey, Self-cleaning surfaces-virtual realities, Nat. Mater. **2**, 301 (2003).

[18] J. Hong, Y. K. Kim, D. J. Won, J. Kim, and S. J. Lee, Three-dimensional digital microfluidic manipulation of droplets in oil medium, Sci. Rep. **5**, 1 (2015).

[19] G. Manukyan, J. M. Oh, D. Van Den Ende, R. G. H. Lammertink, and F. Mugele, Electrical Switching of Wetting States on Superhydrophobic Surfaces: A Route Towards Reversible Cassie-to-Wenzel Transitions, Phys. Rev. Lett. **106**, 014501 (2011).

[20] K. Xiao, X. Chen, and C. X. Wu, Electric field-triggered Cassie-Baxter-Wenzel wetting transition on textured surface, Phys. Rev. Res. **3**, 033277 (2021).

[21] R. Yan and C. L. Chen, Condensation droplet distribution regulated by electrowetting, J. Heat Transfer **141**, 111501 (2019).

[22] J. Li and C. J. Kim, Current commercialization status of electrowetting-on-dielectric (EWOD) digital microfluidics, Lab Chip **20**, 1705 (2020).

[23] P. Teng, D. Tian, H. Fu, and S. Wang, Recent progress of electrowetting for droplet manipulation: From wetting to superwetting systems, Mater. Chem. Front. **4**, 140 (2020).

[24] X. Rui, S. Song, W. Wang, and J. Zhou, Applications of electrowetting-on-dielectric (EWOD) technology for droplet digital PCR, Biomicrofluidics **14**, 1 (2020).

[25] V. Jain, R. K. Dwivedi, and K. Muralidhar, Closed EWOD-based low-cost portable thermal detection system for point-of-care applications, Sens. Actuators, A **346**, 113831 (2022).

[26] H. J. J. Verheijen and M. W. J. Prins, Reversible electrowetting and trapping of charge: Model and experiments, Langmuir **15**, 6616 (1999).

[27] A. G. Papathanasiou and A. G. Boudouvis, Manifestation of the connection between dielectric breakdown strength and contact angle saturation in electrowetting, Appl. Phys. Lett. **86**, 1 (2005).

[28] D. Klarman and D. Andelman, A model of electrowetting, reversed electrowetting, and contact angle saturation, Langmuir **27**, 6031 (2011).

[29] H. A. A. Ali, H. A. Mohamed, and M. Abdelgawad, Repulsion-based model for contact angle saturation in electrowetting, Biomicrofluidics **9**, 1 (2015).

[30] A. G. Papathanasiou, A. T. Papaioannou, and A. G. Boudouvis, Illuminating the connection between contact angle saturation and dielectric breakdown in electrowetting through leakage current measurements, J. Appl. Phys. **103**, 034901 (2008).

[31] X. Li, H. Tian, J. Shao, Y. Ding, X. Chen, L. Wang, and B. Lu, Decreasing the saturated contact angle in electrowetting-on-dielectrics by controlling the charge trapping at liquid-solid interfaces, Adv. Funct. Mater. **26**, 2994 (2016).

[32] Q. Vo and T. Tran, Dynamics of droplets under electrowetting effect with voltages exceeding the contact angle saturation threshold, J. Fluid Mech. **925**, A19 (2021).

[33] P. G. De Gennes, Wetting: Statics and dynamics, Rev. Mod. Phys. **57**, 827 (1985).

[34] R. K. Dwivedi, V. Jain, and K. Muralidhar, Dynamic contact angle model for resolving low-viscosity droplet oscillations during spreading over a surface with varying wettability, Phys. Rev. Fluids **7**, 034002 (2022).

[35] M. Schneemilch, W. J. J. Welters, R. A. Hayes, and J. Ralston, Electrically induced changes in dynamic wettability, Langmuir **16**, 2924 (2000).

[36] See Supplemental Material at http://link.aps.org/supplemental/10.1103/PhysRevE.106.045111 for surface characterization of FluoroPel-coated glass and discussion of PDMS. Captions of the multimedia views of electrowetting videos are listed. It includes a discussion on hysteresis as a dynamic property in numerical simulation whose selection influences match with experiments.

[37] J. H. Kim, P. Kavehpour, and J. P. Rothstein, Dynamic contact angle measurements on superhydrophobic surfaces, Phys. Fluids **27**, 032107 (2015).

[38] C. Renaud, J. M. Cros, Z. Q. Feng, and B. Yang, The Yeoh model applied to the modeling of large deformation contact/impact problems, Int. J. Impact Eng. **36**, 659 (2009).

[39] J. H. Chen and W. H. Hsieh, Electrowetting-induced capillary flow in a parallel-plate channel, J. Colloid Interface Sci. **296**, 276 (2006).

[40] Q. Wang, M. Xu, C. Wang, J. Gu, N. Hu, J. Lyu, and W. Yao, Actuation of a nonconductive droplet in an aqueous fluid by reversed electrowetting effect, Langmuir **36**, 8152 (2020).

[41] A. L. Biance, C. Clanet, and D. Quéré, First steps in the spreading of a liquid droplet, Phys. Rev. E. **69**, 016301 (2004).

[42] I. S. Bayer and C. M. Megaridis, Contact angle dynamics in droplets impacting on flat surfaces with different wetting characteristics, J. Fluid Mech. **558**, 415 (2006).

[43] J. C. Baret, M. M. J. Decré, and F. Mugele, Self-excited drop oscillations in electrowetting, Langmuir **23**, 5173 (2007).

[44] D. A. Saville, Electrohydrodynamics: The Taylor-Melcher leaky dielectric model, Annu. Rev. Fluid Mech. **29**, 27 (1997).